Article

Chiral laser gyroscopes breaking the lock-in limit

https://doi.org/10.1038/s41586-026-10684-4

Received: 18 June 2025

Accepted: 20 May 2026

Published online: 24 June 2026

Open access

Check for updates

Yuan-Hao Mao[1,2,8] ✉, Ji-Peng Xu[2,3,8] ✉, Hong-Teng Ji[2,8], Li-Tian Yang[2], Zhong-Qi Tan[2], Yu-Chuan Quan[4], Tao Pu[1], Wei Shao[1], Jun-Quan Hu[1], Ran Huang[5], Franco Nori[5] ✉ & Hui Jing[6,7] ✉

Ring laser gyroscopes (RLGs) measure rotation via the Sagnac effect: a slight difference in the frequency of the two counter-propagating beams within the resonator. However, at low rotation rates, an intrinsic limitation in RLGs, known as the lock-in phenomenon, counteracts this effect, precluding the widespread adoption of RLGs as motion sensors. Past efforts to avoid this phenomenon include mechanical dithering[1] and magneto-optic non-reciprocity techniques[2]. Such techniques require external components that limit the miniaturization of RLGs. Here we present a self-biased method that overcomes this limitation through chiral spontaneous symmetry breaking and nonlinear frequency pulling in a He–^{20}Ne RLG without inserted elements. Supported by a theoretical model that reveals phase transition conditions with spontaneous symmetry breaking and the dynamics of bistable chiral states, our experiments demonstrate deterministic chirality switching synchronized with rotation direction. Remarkably, the chiral RLG has a linear frequency response at near-zero rotation rates, achieving an open-loop bias instability of 2.2×10^{-2} degrees per hour at a 10 s integration time. Our work presents a strategy for the development of all-solid-state, high-precision and miniaturized laser gyroscopes, which could be used for the exploration of the interplay of nonlinear dynamics and spontaneous symmetry breaking in photonic systems.

The ring laser gyroscope (RLG)—as a mainstream product dominating the high-end inertial sensor market for decades[3,4]—has consistently played a pivotal role in ultra-high-precision inertial navigation systems, autonomous navigation platforms and even fundamental scientific facilities[5–10]. Distinguished from other optical gyroscopes, the RLG's most distinctive feature lies in the integration of the light source and sensing: it is essentially a He–Ne laser, that, at the same time, produces a beat frequency proportional to the rotational rate Ω. This beating signal originates from the Sagnac effect[11,12], which causes a frequency splitting between a pair of clockwise (CW) and counterclockwise (CCW) laser modes (that is, $\Omega_S = S\Omega/2$, where Ω_S is the mode frequency shift and S is a scale factor). However, under low rotation rates, the frequencies of the CW and CCW modes are inevitably degenerate owing to backscattering coupling[13,14], which consequently leads to the loss of the beat signal. This is a fundamental challenge intrinsic to laser gyroscopes known as the lock-in effect.

The current approaches for overcoming the lock-in effect involve two established techniques: the two-frequency mechanical dithered RLG[1] and the magneto-optically biased four-frequency differential RLG[2]. However, both biasing approaches rely on external components (dithering motor and magneto-optic crystals), the reliability of which faces challenges in harsh environments (for example, deep-space exploration), as well as miniaturization and integration demands of high-precision inertial navigation devices[15–19]. An alternative self-biasing concept (that is, without external components) has been proposed[20,21], exploiting intensity-dependent nonlinear interactions among asymmetric multi-longitudinal modes (for example, strong TEM_{00} modes and weak TEM_{01} modes). However, its practical implementation remains elusive due to its complex multi-mode dynamics and unresolved engineering challenges. Notably, asymmetric phenomena are ubiquitous in optical chiral systems[22], which provide an additional degree of freedom for light manipulation[23], computing[24] and sensing[25], enabling transformative applications ranging from chiral logic gates[26], light–matter interactions[27–29] and metamaterial engineering[30,31] to quantum non-reciprocity control[32,33]. Among these diverse forms of asymmetry and chirality in nature and frontier research, this work, as shown in Fig. 1a, focuses on breaking the intensity symmetry of counter-propagating modes in a RLG under single-longitudinal-mode operation via chiral spontaneous symmetry breaking (SSB)[34,35], thereby creating a fundamentally simpler, self-biased chiral laser gyroscope.

Chiral SSB

Recent studies[36–41] have demonstrated that SSB can be achieved through the Kerr nonlinear effect or exceptional points in solid optical systems, and mainly focused on unidirectional light transmission or asymmetric

[1]College of Communications Engineering, Army Engineering University of PLA, Nanjing, China. [2]College of Advanced Interdisciplinary Studies, National University of Defense Technology, Changsha, China. [3]Frontiers Science Center for Nano-optoelectronics and State Key Laboratory for Mesoscopic Physics, School of Physics, Peking University, Beijing, China. [4]Huaguan Technology, Changsha, China. [5]Quantum Information Physics Theory Research Team, Center for Quantum Computing (RQC), RIKEN, Wakoshi, Japan. [6]College of Science, National University of Defense Technology, Changsha, China. [7]Key Laboratory of Low-Dimensional Quantum Structures and Quantum Control of Ministry of Education, Department of Physics, Hunan Normal University, Changsha, China. [8]These authors contributed equally: Yuan-Hao Mao, Ji-Peng Xu, Hong-Teng Ji. ✉e-mail: maoyh96@outlook.com; xujipeng14@nudt.edu.cn; fnori@riken.jp; jinghui73@foxmail.com

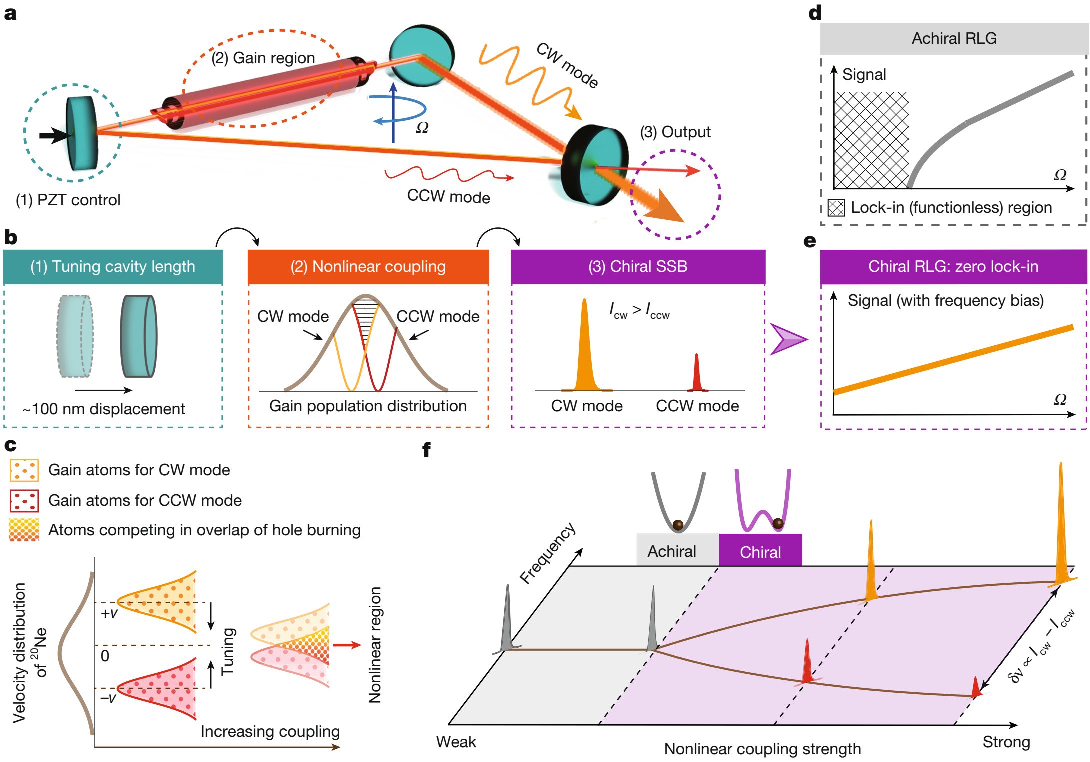

Fig. 1 | Operating principle of a chirality-biased He–^{20}Ne RLG. a, The ring resonator is filled with He–^{20}Ne single-isotope gain gas. The mirror associated with the piezoelectric transducer (PZT) enables nanometre-level cavity length tuning, with a total tuning range of over 3 µm. The intensity of the chiral CW and CCW modes can be observed from the output mirror. **b**, Three steps induce the chirality. First, the laser frequency is shifted towards the gain centre of the ^{20}Ne atoms via cavity length tuning (for example, a 100 nm displacement corresponds to about 126 MHz of frequency tuning in this cavity). Second, overlapping of mirror-image spectral hole burning near the gain centre induces nonlinear mode coupling. Third, nonlinear coupling triggers chiral SSB (I_{cw}/I_{ccw}, the intensity of the CW or CCW laser modes). **c**, Key mechanism of enhanced nonlinear coupling. The CW or CCW modes are usually independently excited in distinct atomic subpopulations, while they are forced to compete for shared gain atoms within the overlap of spectral hole burning near the ^{20}Ne gain centre. The overlap area governs the nonlinear coupling strength. **d**, The lock-in effect in an achiral RLG causes signal extinction at low rotation rates. **e**, The chiral RLG generates frequency bias through SSB, eliminating the lock-in. **f**, Schematic of the SSB transition from achiral (degenerate modes) to chiral state (intensity and frequency splitting modes) with increasing nonlinear coupling strength. The frequency splitting of CW and CCW laser modes $\delta\nu$ is proportional to the intensity difference $I_{cw} - I_{ccw}$.

laser emission. Here we induce SSB directly by mode competitions in a He–^{20}Ne single-isotope gas laser (Fig. 1b,c). Contrary to the achiral RLGs restricted by the lock-in region (Fig. 1d), the chirality-biased RLG is able to break the lock-in limit by spontaneous frequency splitting (as depicted in Fig. 1e and the purple region of Fig. 1f).

Using a two-parameter phase diagram analysis within a third-order nonlinear dynamic formalism[42–44] (Methods), we theoretically demonstrate the spontaneous symmetry-breaking phenomenon in ring laser systems via numerical modelling. Figure 2a reveals the dependence of the steady-state mode intensity on the pump current I_p and ξ through the dynamic analysis; the yellow curve demarcates the parameter boundaries for SSB phase transitions in the ring laser system. Simulated results reveal that a significant intensity disparity between CW and CCW outputs occurs when both the gain and coupling strength exceed critical thresholds (as derived in the Methods), which is crucial for our chirality-biased operating principle.

To facilitate a direct comparison with experimental data, we also illustrate in Fig. 2b,d the symmetry-breaking process by varying the pump current I_p and nonlinear coupling strength ξ independently, along the dashed lines in Fig. 2a. The corresponding experimental data is shown in Fig. 2c,e, in which ξ is finely controlled by the cavity tuning. Their close agreement confirms the feasibility of inducing SSB via operational parameter optimization in He–^{20}Ne ring lasers.

Notably, Fig. 2b,c demonstrates an anomalous intensity decrease in the CCW mode with increasing gain after the phase transition, whereas the sum of the CW and CCW mode intensities still increases with the pump. To clarify this phenomenon, we numerically tracked the dynamical evolution of the CW or CCW modes before and after SSB. Figure 2f,g shows that in the symmetric phase, all trajectories converge to a unique stable fixed point, S_0, located at the $I_{cw} = I_{ccw}$ curve, regardless of the relative relationship between i_{cw} and i_{ccw} (i_{cw} and i_{ccw} denote the initial intensity of the CW and CCW laser modes respectively). By contrast, Fig. 2h reveals bistable fixed points (S_1 and S_2) in the chiral SSB phase, where the mode with a larger initial value will eventually form a stable strong mode as depicted by green arrows at $I_p = 0.6$ mA. Remarkably, as shown in Fig. 2i, a mere 0.1% initial intensity advantage of the CW mode over the CCW mode (that is, $i_{cw} = (1 + 0.1\%)i_{ccw}$) suffices to establish a stable CW mode-dominant state.

Controlled versus random chiral SSB

As shown in Fig. 3a, to experimentally study the chiral SSB phase in a two-frequency RLG (that is, only a single longitudinal mode oscillates in both CW and CCW directions), we fabricated a triangular He–^{20}Ne RLG with a side length of 125 mm. Its cavity supports a free spectral range of 800 MHz at 632.8 nm and is mounted horizontally on a rotation stage. A direct current power supply connected to one cathode and two anodes is used to pump the He–^{20}Ne laser. Beat frequency signals between the CW and CCW laser modes are detected through the beam-combining prism port, whereas the other port enables the observation of CW or CCW intensity along distinct spatial directions. As shown in Fig. 3b, when the RLG operates in the chiral SSB phase, a

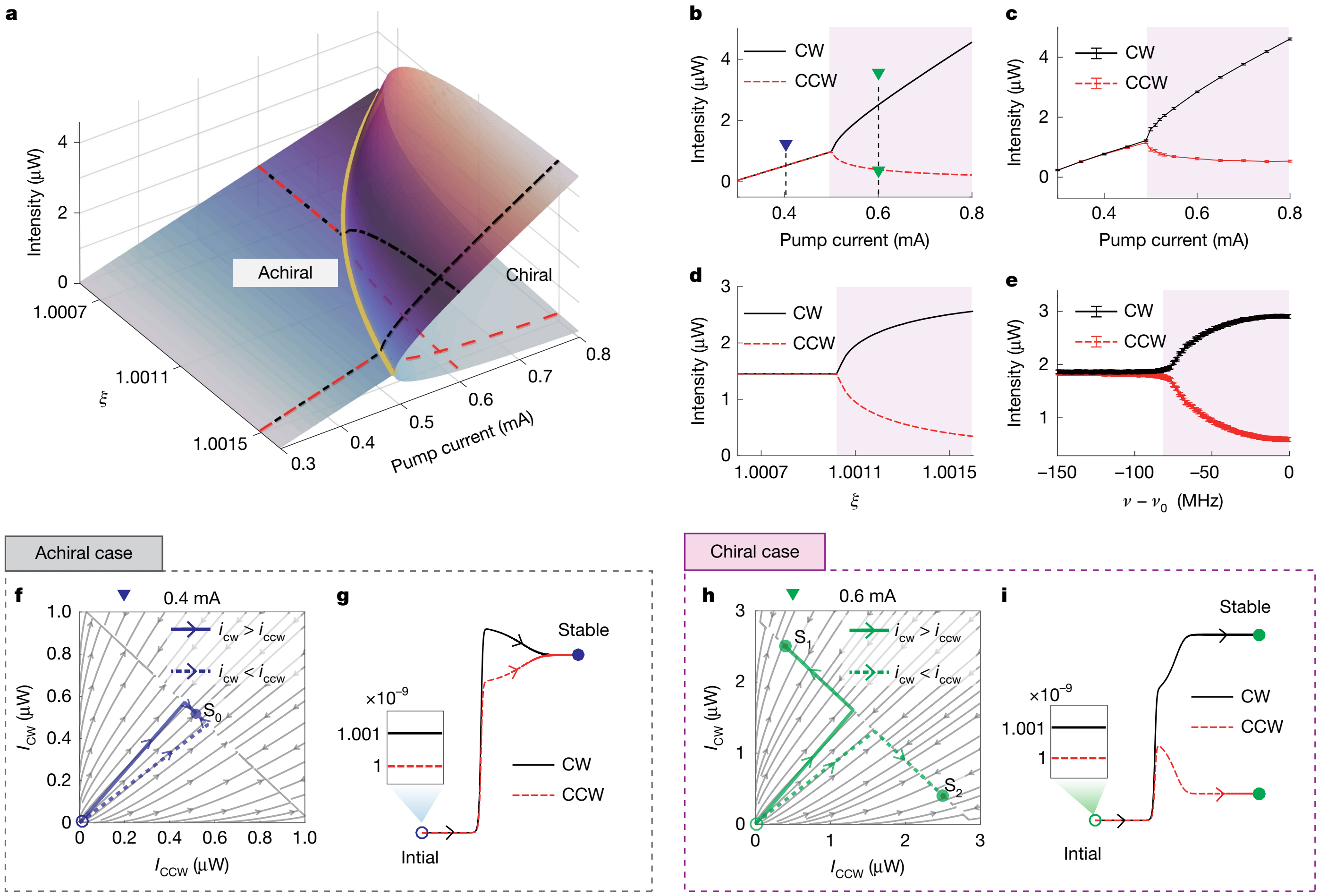

Fig. 2 | Theoretical analysis of SSB in the ring laser. a, Phase diagram in two-parameter space (where ξ is the nonlinear coupling coefficient) demarcating symmetric (left of the yellow curve) and chiral SSB states (right). **b**,**c**, Simulated (**b**) and experimental (**c**) results of pitchfork bifurcation in CW or CCW intensities by increasing gain at $\xi = 1.0015$ and $\nu = \nu_0$; ν_0 is the gain centre of ^{20}Ne. **d**,**e**, Simulated (**d**) and experimental (**e**) results of pitchfork bifurcation by increasing the nonlinear coupling coefficient (or tuning frequency) at the pump current $I_p = 0.6$ mA. Pink background shading in **b**–**e** represents the transition from achirality to chirality. **f**,**h**, Simulations of the symmetric state ($I_p = 0.4$ mA) (**f**) and the chiral SSB state ($I_p = 0.6$ mA) (**h**). **f**, Phase diagram of the intensity evolution with one stable point (S_0). **h**, Phase diagram of the intensity evolution with two stable points (S_1 and S_2), where i_{cw} and i_{ccw} are the minute initial intensities of the CW and CCW modes, respectively. **g**,**i**, Schematics of the evolution of the CW and CCW mode intensities from the initial to the stable state under symmetric (**g**) and chiral (**i**) SSB conditions. In both **g** and **i**, i_{cw} exceeds i_{ccw} by 0.1%. Data in **c** and **e** are presented as mean ± s.d. ($n = 100$ independent experiments).

chirality switch can be observed by a slight disturbance (for example, a sudden vibration of the platform) under stationary conditions (no rotation). This phenomenon serves as direct evidence for the existence of bistability in the chiral system. The following analysis will elucidate the switching dynamics of this bistable state under both stationary and rotating conditions.

First, a random chirality can be induced by power cycling under the stationary condition. Before the experiment, we stabilized the system in the chiral SSB phase by fixing both pump current and operating point, with the rotation stage disabled. Numerical results in Fig. 2h reveal that the final chiral state critically depends on the initial mode intensity in the chiral SSB phase. For He–Ne ring lasers, these initial conditions are fundamentally stochastic due to spontaneous emission noise. Consequently, as shown in Fig. 3c, each power restart generates random chiral output selection. To quantify this randomness, 200 consecutive power-restarting cycles are performed. Statistical analysis in Fig. 3d confirms equal probabilities for both chiral states.

Second, a controllable chirality switch can be induced by the rotation. Under continuous pumping, we implement a rotational modulation by oscillating the stage with an angular speed of ±0.1 degrees per second. As shown in Fig. 3e, directional inversion of the rotational stage induces a synchronized chirality switch. Specifically, the direction of the dominant modes is consistent with the rotation direction of the RLG. Under fixed gain and operating point, 200 directional transitions are statistically analysed, revealing a near-perfect correlation between rotation direction and output chirality in Fig. 3f.

Experimental demonstration of chirality-biased RLG

Compared with traditional two-frequency RLGs, the beat frequency of the chiral RLG needs to be modified as equation (1): (the derivation can be found in the Methods)

$$\Delta\nu = \sqrt{[\eta(I_{cw} - I_{ccw}) + 2\Omega_S]^2 - \left(\frac{I_{cw}}{I_{ccw}} + \frac{I_{ccw}}{I_{cw}} + 2\right) r^2} \qquad (1)$$

where $\Delta\nu$ is the beat frequency of the chiral RLG; r is the backscattering coupling coefficient; η is the nonlinear frequency pulling coefficient (refer to the Supplementary Information for the derivation), which represents the overall effect of the laser intensity on its own frequency.

Benefiting from common-mode noise suppression, conventional RLGs can directly extract the Sagnac frequency splitting from the beat

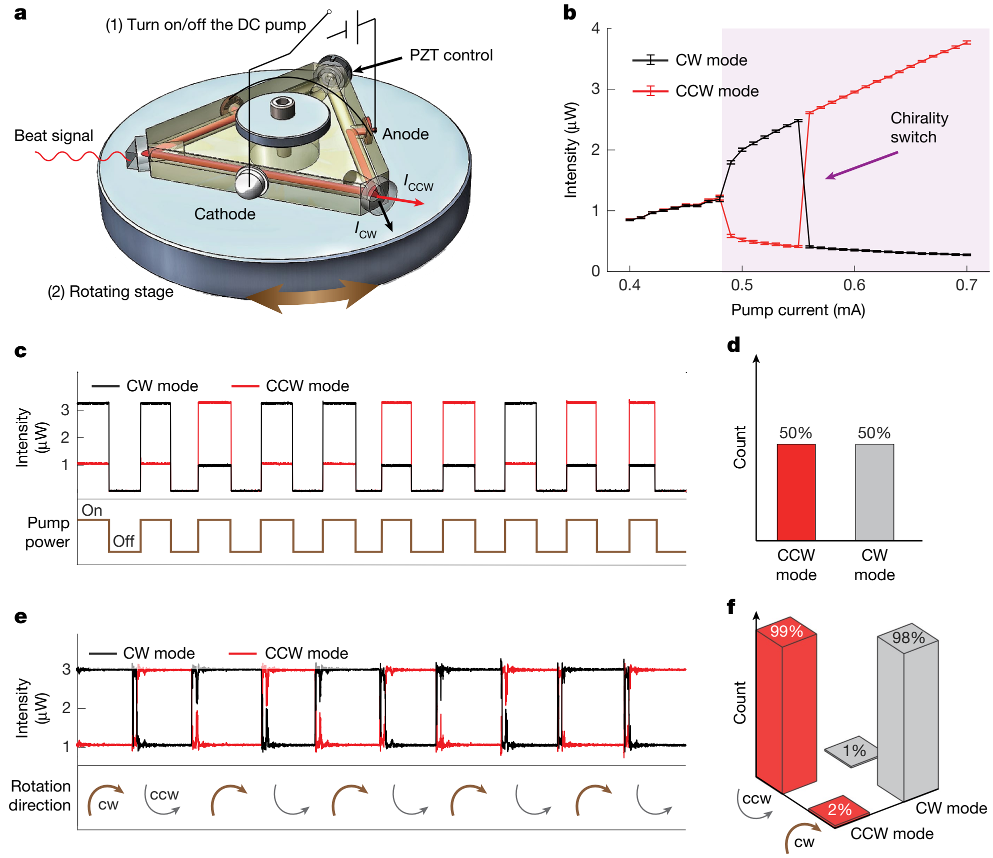

Fig. 3 | Chirality switch in the chiral SSB phase of a He–^{20}Ne RLG. **a**, Experimental set-up. Two methods, (1) turning the DC pump on/off and (2) rotating the stage, are applied to induce a change in the chirality. **b**, Existence of bistable chirality in the chiral SSB phase under the stationary condition. Data are presented as mean ± s.d. (n = 100 independent experiments). **c**,**d**, Random chirality selections observed during periodic power cycling of the RLG (**c**) and its corresponding statistical results (**d**). **e**,**f**, Regular and controllable chirality switches with uniform periodic oscillations of the RLG (**e**) and its corresponding statistical results (**f**). The statistical analyses for **d** and **f** are based on 200 experimental runs, and only the modes with higher intensity are counted in each run.

signal with balanced CW and CCW intensities, whereas equation (1) demonstrates that the intensity-dependent nonlinear frequency pulling introduces an additional term $\eta(I_{cw}-I_{ccw})$ when $I_{cw} \neq I_{ccw}$. Considering a typical value of the backscattering coefficient r = 30 Hz, for a chiral RLG operating at the point of maximum frequency bias (for example, $v = v_3$ in Fig. 4a) with an intensity ratio $I_{cw}/I_{ccw} \approx 2.4$, the introduced frequency bias is about 364 Hz, which is far greater than the lock-in threshold $\sqrt{\left(\frac{I_{cw}}{I_{ccw}}+\frac{I_{ccw}}{I_{cw}}+2\right)}\,r \approx 66$ Hz. The chiral RLG will therefore always have a real and nearly linear frequency response with rotation, provided that $\eta(I_{cw}-I_{ccw})$ and Ω_S have the same sign. Moreover, although the intensity asymmetry at this operating point reduces the interference fringe contrast by approximately 10%, leading to a decrease in the signal-to-noise ratio from 35.5 dB under achiral conditions to 34.9 dB under chiral conditions, this value remains well above the typical SNR limit (about 20 dB) required for high-precision laser gyroscope frequency counting. Therefore, such a chiral bias does not adversely affect the readout of the gyroscope signal.

Further experiments were conducted to investigate the correlation between chiral SSB and the frequency bias in the He–^{20}Ne RLG. The laser gyroscope rotates clockwise at 0.5 degrees per second with a fixed pumping power. As shown in Fig. 4a, the strong mode coupling induced by continuous frequency tuning around the ^{20}Ne gain centre v_0 drives the RLG operating in the chiral SSB phase, where the CW mode intensity dominates ($I_{cw} > I_{ccw}$). The grey dashed line in the upper panel of Fig. 4a reveals the odd symmetry of the nonlinear frequency pulling coefficient η with respect to v_0 (refer to the Supplementary Information for a derivation). This nonlinear effect pulls the laser line to the gain centre, independent of which one has a higher frequency.

To validate the linear response of the chiral RLG in the lock-in region, three operating points (that is, $v_1 \approx v_3$ in Fig. 4a) are tested under the chiral SSB phase. As depicted in Fig. 4b, the measured frequency responses show excellent linearity from −0.5 to +0.5 degrees per second, differing only in the frequency bias values. In contrast, when the operating point is tuned to v_a, as shown in Fig. 4a, the gyroscope operating in the normal achiral state has a nonlinear frequency response at rotation speeds below 0.05 degrees per second and enters the lock-in region when Ω is lower than 0.03 degrees per second. Notably, a chirality flip occurs concurrently with the reversal of the rotation direction, which is consistent with the experimental results presented in Fig. 3e. Furthermore, to comprehensively validate the effect of chirality on the frequency bias, the chirality is artificially switched (such as restarting the power supply with a directional seed light) during clockwise rotation. As indicated by the thumbs-down region in Fig. 4b, this chirality-switched state produces a significant negative frequency bias, which in turn substantially increases the lock-in threshold of the RLG. The dashed curves in Fig. 4b show theoretical predictions from equation (1), demonstrating excellent agreement with experimental measurements.

With a fixed operating point v of the RLG, Fig. 4c illustrates the principle of how the frequency bias remains positive and the reason why the chirality switches when the rotation direction is reversed. First, the Sagnac effect causes opposite frequency shifts in CW and CCW laser modes. The travelling mode with the same direction as the rotation has

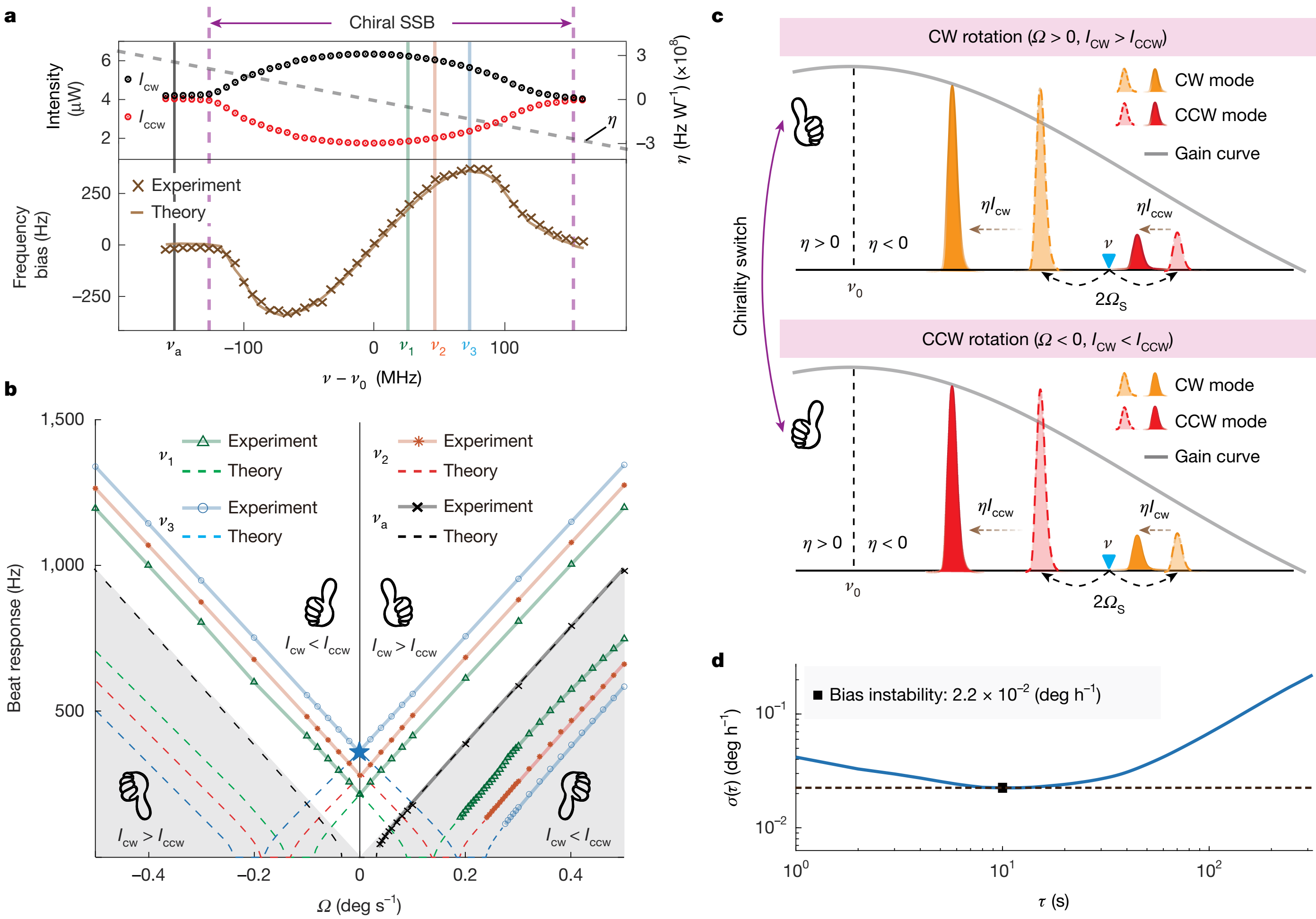

Fig. 4 | Frequency response characteristics of the chiral RLG. a, The CW or CCW mode intensity, nonlinear frequency pulling coefficient η (top) and the corresponding frequency bias with tuning frequency ν around the ^{20}Ne gain centre ν_0 (bottom). **b**, The frequency response to low rotational speed of the RLG under different operating points and chirality states. Here, ν_1, ν_2 and ν_3 denote the chiral states and ν_a corresponds to the achiral state. **c**, Schematic of chirality switch and frequency bias principles for the RLG under CW or CCW rotation conditions. Ω_S is the frequency shift caused by the Sagnac effect. **d**, Allan variance analysis of a 1,000 s frequency bias stability test at the operating point indicated by the blue star in **b**.

a longer optical path, corresponding to a lower resonant frequency. Conversely, the resonant frequency is higher. When the operating frequency ν exceeds ν_0, the frequency-downshifted mode gains higher amplification due to the gain profile. As a result, this laser mode is more likely to acquire a relatively large initial value and thus evolves into a strong mode. Similarly, the change of rotation direction will reverse the frequency shift induced by the Sagnac effect, which consequently leads to a chirality switch. Furthermore, negative η values induce intensity-dependent frequency pulling toward ν_0. For instance, as shown in the upper panel of Fig. 4c, the dominant CW mode has stronger pulling than the weaker CCW mode, generating a positive frequency bias.

To evaluate chirality-biased stability, the chiral RLG is horizontally mounted on a vibration-isolated granite platform, with its operating point fixed at the position where the frequency bias is maximum (that is, $\nu = \nu_3$ shown in Fig. 4a). Conventional two-frequency RLGs with comparable dimensions would operate below the lock-in threshold with complete signal extinction. Strikingly, as indicated by the blue star in Fig. 4b, our chiral RLG outputs a stable 364.4 Hz beat signal under identical conditions. Its corresponding Allan variance analysis, shown in Fig. 4d, reveals a bias instability of 2.2×10^{-2} degrees per hour with 10 s of integration time over 1,000 s open-loop operation—three orders of magnitude below Earth's rotation rate (around 15 degrees per hour)—confirming robust chiral SSB phase with precise constant frequency bias.

In fact, as the He–Ne RLG is a typical Doppler-broadening dominant gas laser system, pioneering research[45] revealed that strong coupling in neon single-isotopes would extinguish one propagation direction (that is, complete chirality), thereby eliminating angular velocity sensing. Consequently, conventional RLGs have long used dual-isotope gas mixtures (^{20}Ne and ^{22}Ne) to avoid bidirectional mode coupling, inadvertently precluding exploration of chiral SSB in He–Ne ring lasers. Our work revisits this fundamental mechanism by using ^{20}Ne single-isotope gas, leveraging strong CW or CCW mode coupling under single-longitudinal-mode conditions to induce stable SSB through hole-burning effects. Furthermore, compared with traditional RLGs, the higher gas pressure (7–9 torr) and ultra-low cavity loss (<100 ppm) enabled by precision fabrication[46] are critical for achieving controllable and stable chiral output (Methods and Supplementary Information).

Conclusion

Here we have developed a new chirality-biased RLG based on chiral SSB, which eliminates the longstanding lock-in problem. By exploiting nonlinear mode interactions in a He–^{20}Ne single-isotope RLG, we have achieved stable chiral states with intensity-dependent frequency pulling, enabling a robust linear response even at near-zero rotation rates. Experimental validation of a 0.02 degrees per hour bias instability under open-loop operation highlights the technology's readiness for high-precision navigation applications. Furthermore, the deterministic control of frequency bias via operational SSB phases opens new avenues for exploring nonlinear dynamics in photonic systems. This demonstration redefines the design principles of RLGs by showing that controllable strong coupling between laser modes leads to a state-of-the-art application rather than chaotic mode competition. It is noteworthy that the chirality-induced frequency bias is sensitive to operating point and gain fluctuations, a consideration that becomes critical for on-chip implementations where thermal effects may induce drift. Therefore, transitioning to integrated platforms would require robust gain control and advanced frequency stabilization to ensure stability and reproducibility.

In summary, this work bridges fundamental research in symmetry breaking with next-generation inertial sensing technologies, promising transformative impacts across metrology[47], integrated photonics[48,49] and quantum precision sensing systems[50,51].

Online content

Any methods, additional references, Nature Portfolio reporting summaries, source data, extended data, supplementary information, acknowledgements, peer review information; details of author contributions and competing interests; and statements of data and code availability are available at https://doi.org/10.1038/s41586-026-10684-4.

1. Killpatrick, J. The laser gyro. *IEEE Spectr.* **4**, 44–55 (1967).
2. Statz, H., Dorschner, T. A., Holtz, M. & Smith, I. W. in *Laser Handbook* 229–332 (Elsevier, 1985); https://doi.org/10.1016/B978-0-444-86927-2.50007-3.
3. Chow, W. W. et al. The ring laser gyro. *Rev. Mod. Phys.* **57**, 61–104 (1985).
4. Passaro, V. M. N., Cuccovillo, A., Vaiani, L., De Carlo, M. & Campanella, C. E. Gyroscope technology and applications: a review in the industrial perspective. *Sensors* **17**, 2284 (2017).
5. Di Virgilio, A. D. V. et al. Underground Sagnac gyroscope with sub-prad/s rotation rate sensitivity: toward general relativity tests on Earth. *Phys. Rev. Res.* **2**, 032069 (2020).
6. Capozziello, S. et al. Constraining theories of gravity by GINGER experiment. *Eur. Phys. J. Plus* **136**, 394 (2021).
7. Benisty, D., Brax, P. & Davis, A.-C. Multiscale constraints on scalar-field couplings to matter: The geodetic and frame-dragging effects. *Phys. Rev. D* **108**, 063031 (2023).
8. Igel, H. et al. ROMY: a multicomponent ring laser for geodesy and geophysics. *Geophys. J. Int.* **225**, 684–698 (2021).
9. Schreiber, K. U., Kodet, J., Hugentobler, U., Klügel, T. & Wells, J. R. Variations in the Earth's rotation rate measured with a ring laser interferometer. *Nat. Photon.* **17**, 1054–1058 (2023).
10. Giovinetti, F. et al. GINGERINO: a high sensitivity ring laser gyroscope for fundamental and quantum physics investigation. *Front. Quantum Sci. Technol.* **3**, 1363409 (2024).
11. POST, E. J. Sagnac effect. *Rev. Mod. Phys.* **39**, 475–493 (1967).
12. Wilkinson, J. R. Ring lasers. *Prog. Quantum Electron.* **11**, 1–103 (1987).
13. Scully, M. O. & Zubairy, M. S. *Quantum Optics* (Cambridge Univ. Press, 1997).
14. Yan, S. et al. Lock-in phenomena in non-Hermitian coupled systems. *Opt. Commun.* **546**, 129760 (2023).
15. Li, J., Suh, M.-G. & Vahala, K. Microresonator Brillouin gyroscope. *Optica* **4**, 346 (2017).
16. Liang, W. et al. Resonant microphotonic gyroscope. *Optica* **4**, 114 (2017).
17. Gundavarapu, S. et al. Sub-hertz fundamental linewidth photonic integrated Brillouin laser. *Nat. Photon.* **13**, 60–67 (2019).
18. Lai, Y. H. et al. Earth rotation measured by a chip-scale ring laser gyroscope. *Nat. Photon.* **14**, 345–349 (2020).
19. Liu, D. et al. All-solid-state miniature laser gyroscope based on a single monolithic non-planar ring oscillator. *Photon. Res.* **13**, 897 (2025).
20. Scully, M. O., Sanders, V. & Sargent, M. Novel multioscillator approach to the problem of locking in two-mode ring-laser gyros. *Opt. Lett.* **3**, 43 (1978).
21. Anderson, D. Z., Sanders, V. E., Chow, W. W. & Scully, M. O. Optically biased laser gyro. *Opt. Lett.* **5**, 413 (1980).
22. Bliokh, K. Y. & Nori, F. Characterizing optical chirality. *Phys. Rev. A* **83**, 021803 (2011).
23. Hayat, A., Mueller, J. P. B. & Capasso, F. Lateral chirality-sorting optical forces. *Proc. Natl Acad. Sci. USA* **112**, 13190–13194 (2015).
24. Söllner, I. et al. Deterministic photon-emitter coupling in chiral photonic circuits. *Nat. Nanotechnol.* **10**, 775–778 (2015).
25. Yoo, S. J. & Park, Q. H. Metamaterials and chiral sensing: a review of fundamentals and applications. *Nanophotonics* **8**, 249–261 (2019).
26. Zhang, Y. et al. Chirality logic gates. *Sci. Adv.* **8**, eabq8246 (2022).
27. Tang, Y. & Cohen, A. E. Optical chirality and its interaction with matter. *Phys. Rev. Lett.* **104**, 1–4 (2010).
28. Bliokh, K. Y. & Nori, F. Transverse and longitudinal angular momenta of light. *Phys. Rep.* **592**, 1–38 (2015).
29. Xiao, T. H. et al. All-dielectric chiral-field-enhanced Raman optical activity. *Nat. Commun.* **12**, 1–7 (2021).
30. Zhang, X., Liu, Y., Han, J., Kivshar, Y. & Song, Q. Chiral emission from resonant metasurfaces. *Science* **377**, 1215–1218 (2022).
31. Deng, H. et al. Chiral lasing enabled by strong coupling. *Sci. Adv.* **11**, eads9562 (2025).
32. Zhang, Z. et al. Chirality-induced quantum non-reciprocity. *Nat. Photon.* **19**, 840–846 (2025).
33. Lodahl, P. et al. Chiral quantum optics. *Nature* **541**, 473–480 (2017).
34. Minganti, F., Arkhipov, I. I., Miranowicz, A. & Nori, F. Liouvillian spectral collapse in the Scully-Lamb laser model. *Phys. Rev. Res.* **3**, 043197 (2021).
35. Minganti, F., Arkhipov, I. I., Miranowicz, A. & Nori, F. Continuous dissipative phase transitions with or without symmetry breaking. *New J. Phys.* **23**, 122001 (2021).
36. Hamel, P. et al. Spontaneous mirror-symmetry breaking in coupled photonic-crystal nanolasers. *Nat. Photon.* **9**, 311–315 (2015).
37. Cao, Q. T. et al. Experimental demonstration of spontaneous chirality in a nonlinear microresonator. *Phys. Rev. Lett.* **118**, 033901 (2017).
38. Cao, Q. T. et al. Reconfigurable symmetry-broken laser in a symmetric microcavity. *Nat. Commun.* **11**, 1–7 (2020).
39. Longhi, S. & Feng, L. Unidirectional lasing in semiconductor microring lasers at an exceptional point [Invited]. *Photon. Res.* **5**, B1 (2017).
40. Chen, Y. et al. Electrically reconfigurable mode chirality in integrated microring resonators. *Laser Photon. Rev.* **18**, 2301289 (2024).
41. Yang, J., Li, H., Yan, S., Gong, Q. & Xu, X. Local high chirality near exceptional points based on asymmetric backscattering. *New J. Phys.* **26**, 093044 (2024).
42. Etrich, C., Mandel, P., Centeno Neelen, R., Spreeuw, R. J. C. & Woerdman, J. P. Dynamics of a ring-laser gyroscope with backscattering. *Phys. Rev. A* **46**, 525–536 (1992).
43. Spreeuw, R. J. C., Neelen, R. C., van Druten, N. J., Eliel, E. R. & Woerdman, J. P. Mode coupling in a He-Ne ring laser with backscattering. *Phys. Rev. A* **42**, 4315–4324 (1990).
44. Sargent, M., Scully, M. O. & Lamb, W. E. J. *Laser Physics* (Westview Press, 1978).
45. Aronowitz, F. Single-isotope laser gyro. *Appl. Opt.* **11**, 405 (1972).
46. Tan, Z., Jiang, X., Mao, Y., Long, X. & Luo, H. Ultra-smooth surface with 0.4 Å roughness on fused silica. *Ceram. Int.* **49**, 7245–7251 (2023).
47. Frérot, I. & Roscilde, T. Symmetry: a fundamental resource for quantum coherence and metrology. *Phys. Rev. Lett.* **133**, 260402 (2024).
48. Xu, G. et al. Spontaneous symmetry breaking of dissipative optical solitons in a two-component Kerr resonator. *Nat. Commun.* **12**, 4023 (2021).
49. Lee, H. et al. Chiral exceptional point enhanced active tuning and nonreciprocity in micro-resonators. *Light Sci. Appl.* **14**, 45 (2025).
50. Kuffer, M., Zwick, A. & Álvarez, G. A. Sensing out-of-equilibrium and quantum non-gaussian environments via induced time-reversal symmetry breaking on the quantum-probe dynamics. *PRX Quantum* **6**, 020320 (2025).
51. Gao, H. et al. Signal amplification in a solid-state sensor through asymmetric many-body echo. *Nature* **646**, 68–73 (2025).

Methods

Fabrication of the He–^{20}Ne single-isotope RLG

The ring cavity of the laser gyroscope is fabricated from a single block of Zerodur glass (coefficient of thermal expansion $\leq 2\times10^{-8}$ K^{-1}; ref. 52), which provides remarkable dimensional stability under temperature variations. For a total cavity length of 0.375 m, a temperature fluctuation of 0.1 °C results in a length change of $\Delta L = 0.375$ m $\times 2\times10^{-8}$ °C^{-1} $\times$ 0.1 °C = 0.75 nm. This corresponds to a frequency drift of less than 1 MHz.

The optical cavity itself ensures a closed optical path through high machining precision, with the angular errors at its three corners controlled within five arcseconds and the length errors of its three sides maintained below 1 μm. Three ultra-smooth mirrors (with a surface roughness, R_a, of below 0.05 nm) were optically bonded to the cavity, achieving a total cavity loss of 68 ppm. Hermetic sealing is implemented through indium-alloy joints for both anode and cathode interfaces.

Before gas filling, the cavity underwent ultra-high vacuum baking at 80–120 °C for 168 h under a base pressure of under 1×10^{-7} torr, effectively removing residual contaminants and ensuring molecular-level cleanliness. Finally, the cavity is filled with a He–^{20}Ne gas mixture under precise flow control, where the total pressure is 8 torr and the ratio of He and ^{20}Ne is 30:1.

Third-order nonlinear dynamic formalism

To elucidate the SSB mechanism in RLGs, we start from the third-order nonlinear dynamic equations for the dissipatively coupled counter-propagating waves:

$$\frac{\partial}{\partial t}\tilde{E}_{1,2} = (\tilde{\alpha} - \tilde{b}E_{1,2}^2 - \tilde{c}E_{2,1}^2)\tilde{E}_{1,2} \pm i\Omega_S\tilde{E}_{1,2} + r\tilde{E}_{2,1} \tag{2}$$

where $\tilde{E}_{1,2}(t) = E_{1,2}(t)\exp[-i(vt+\mu_{1,2}(t))]$ represent the complex electric fields of the CW and CCW waves, with time-dependent amplitudes $E_{1,2}(t)$ and phases $\mu_{1,2}(t)$; v is the resonant frequency of the ring cavity (that is, the operating point of the RLG); Ω_S denotes the frequency shift caused by the Sagnac effect and r is the backscattering coupling coefficient. The real and imaginary parts of the complex parameters ($\tilde{a} = \alpha + i\sigma$, $\tilde{b} = \beta + i\rho$, $\tilde{c} = \theta + i\tau$), detailed in Supplementary Table 1, represent the linear and nonlinear effects on the amplitude and phase, respectively. This allows equation (2) to be decomposed into a set of coupled differential equations for the amplitude and phase. Analysis of the steady-state solutions to the amplitude equations revealed two key parameters governing the chiral behaviour: the pumping power and the operating point (that is, laser frequency), corresponding respectively to the net gain coefficient $\alpha = \mathrm{Re}(\tilde{a})$ and nonlinear coupling coefficient $\xi = \mathrm{Re}(\tilde{c})/\mathrm{Re}(\tilde{b}) = \theta/\beta$. In particular, α is proportional to the pump current I_p (that is, $\alpha = \chi I_p$) within the gain range (for example, 0.3–0.8 mA) studied in this work and ξ reflects the degree of overlap of the hole-burning regions between the CW and CCW laser modes as shown in Fig. 1c.

The laser gyroscope operates under a constant-voltage (~520 V) direct current pump source. The gain is therefore increased by raising the pump current. Specifically, the threshold pump current of the system is $I_p = 0.29$ mA. This gain corresponds to the net cavity loss rate $\alpha_{th} = \gamma_{th} = -\log(1-\delta)/T_{rt} = 5.435\times10^4$ Hz, where $\delta = 68$ ppm is the total cavity loss and $T_{rt} = \Delta L/c$ is the roundtrip time of the laser inside the cavity (ΔL is the cavity length, c is the speed of light). Under small-signal conditions, the gain is approximately linear, and the gain–current relationship can be estimated by the scaling factor $\chi = \alpha/I_p = \alpha_{th}/I_{pth} = 1.875\times10^5$ Hz mA^{-1}.

Derivation of the chiral SSB condition and frequency difference of the chiral RLG

By separating the real and imaginary parts of equation (2), the dynamic equations for the amplitude and phase can be obtained, respectively:

$$\begin{aligned}\dot{E}_1 &= (\alpha - \beta E_1^2 - \theta E_2^2)E_1 + rE_2\cos\Delta u\\ \dot{E}_2 &= (\alpha - \beta E_2^2 - \theta E_1^2)E_2 + rE_1\cos\Delta u\end{aligned} \tag{3}$$

$$\begin{aligned}\dot{\mu}_1 + v &= -\Omega_S + \sigma - \rho E_1^2 - \tau E_2^2 - r\frac{E_2}{E_1}\sin\Delta u\\ \dot{\mu}_2 + v &= \Omega_S + \sigma - \rho E_2^2 - \tau E_1^2 + r\frac{E_1}{E_2}\sin\Delta u\end{aligned} \tag{4}$$

where $\Delta u = \mu_1 - \mu_2$ is the phase difference between the CW and CCW laser modes (detailed definitions and calculations of $\alpha, \beta, \theta, \sigma, \rho$ and τ can be found in the Supplementary Information).

First, the chiral SSB condition can be derived by equation (3). As the laser phase evolves as a fast variable, the phase difference can be approximated by its time-averaged value over the observable timescale. Consequently, we adopt the approximation $\Delta u \approx 0$ in the subsequent calculations, implying that the influence of the phase difference (that is, the rotation of the gyroscope) on the chiral symmetry-breaking phase transition is neglected. Experimental data provided in the Supplementary Information can validate this approximation.

Based on equation (3), the Jacobian matrix of $\dot{E}_1$ and $\dot{E}_2$ is

$$J = \begin{bmatrix}\dfrac{\partial\dot{E}_1}{\partial E_1} & \dfrac{\partial\dot{E}_1}{\partial E_2}\\[2mm] \dfrac{\partial\dot{E}_2}{\partial E_1} & \dfrac{\partial\dot{E}_2}{\partial E_2}\end{bmatrix} = \begin{bmatrix}-3\beta E_1^2 - \beta\xi E_2^2 + \alpha & -2\beta\xi E_1E_2 + r\\ -2\beta\xi E_1E_2 + r & -3\beta E_2^2 - \beta\xi E_1^2 + \alpha\end{bmatrix} \tag{5}$$

When the determinant of the Jacobian matrix is negative:

$$\det(J)|_{E_1=E_2} = \left[\alpha - \frac{(3+\xi)(r+\alpha)}{1+\xi}\right]^2 - \left[r - \frac{2\xi(r+\alpha)}{1+\xi}\right]^2 < 0 \tag{6}$$

the symmetric solution in equation (3) loses stability, but leads to a pitchfork bifurcation of the nonlinear system described in Fig. 2a. Simplifying equation (6), the critical condition of chiral SSB is obtained:

$$\alpha(\xi - 1) > 2r \tag{7}$$

Equation (7) demonstrates that strong coupling ($\xi > 1$) serves as a necessary condition for chirality emergence. The practically attainable ranges of α and ξ fundamentally constrain the design space, necessitating ultra-low background scattering r that can only be achieved through ultra-precise fabrication techniques[46].

Second, a standard Adler equation can be obtained by subtracting the two equations in equation (4):

$$\partial_t\Delta u = A - B\sin\Delta u \tag{8}$$

Solving equation (8), the expression for the phase difference Δu is obtained:

$$\tan(\Delta u/2) = \frac{1}{A}[B + \omega_B\tan(\omega_B t + \varphi_0)] \tag{9}$$

where $\omega_B = \sqrt{A^2 - B^2}/2$ and ϕ_0 is an arbitrary constant. Let $I_{cw} = E_1^2$, $I_{ccw} = E_2^2$ and $\eta = \rho - \tau$. The coefficients A, B in equations (8) and (9) can be written as:

$$A = (\rho - \tau)(E_1^2 - E_2^2) + 2\Omega_S = \eta(I_{cw} - I_{ccw}) + 2\Omega_S,\ B = r\left(\frac{E_2}{E_1} + \frac{E_1}{E_2}\right). \tag{10}$$

The beat frequency Δv is derived by taking the time average (that is, $T = 2\pi/\omega_B$) of the derivative of the phase difference[42]:

$$\Delta v = \frac{1}{T}\int_0^T \frac{\partial \Delta u}{\partial t}dt = \frac{4\pi}{T} = 2\omega_B = \sqrt{A^2 - B^2}$$
$$= \sqrt{[\eta(I_{\mathrm{cw}} - I_{\mathrm{ccw}}) + 2\Omega_S]^2 - \left(\frac{I_{\mathrm{cw}}}{I_{\mathrm{ccw}}} + \frac{I_{\mathrm{ccw}}}{I_{\mathrm{cw}}} + 2\right)r^2}\ . \tag{11}$$

Data availability

The data used to produce the plots in the main figures of this paper are available at https://doi.org/10.6084/m9.figshare.31775725 (ref. 53). Source data are provided with this paper.

Code availability

The main codes supporting this study including those related to simulation, fitting and calculations are available at https://doi.org/10.6084/m9.figshare.31775725 (ref. 53).

52. *Expansion Class 0|SCHOTT* (Schott, 2026); https://www.schott.com/en-us/products/zerodur-p1000269/technical-details.
53. Mao, Y. et al. Dataset for "Chiral laser gyroscopes breaking the lock-in limit". *figshare* https://doi.org/10.6084/m9.figshare.31775725 (2026).

Acknowledgements We acknowledge L. Ge, W. Liu, X. Jiang, S. Chen, C.-G. Chen and S. Zhou for helpful discussions, and Y.-J. Guan and H. Hu for their support on experimental set-ups.

Author contributions Y.-H.M., J.-P.X. and H.J. proposed and designed the research. Y.-H.M., Z.-Q.T. and Y.-C.Q. designed and fabricated the high-quality He–Ne laser resonator. Y.-H.M., J.-P.X., L.-T.Y., H.-T.J., Y.-C.Q., T.P. and W.S. did the chirality measurements and analysed the raw data. Y.-H.M., H.-T.J. and J.-Q.H measured the beat response and long-term stability of the chiral RLG and did the Allan variance analysis. Y.-H.M. and J.-P.X. did the theoretical analysis and simulations with the help of H.J. Y.-H.M., J.-P.X. and H.J. wrote the manuscript with the input of L.-T.Y., R.H. and F.N. All authors discussed the results and commented on the manuscript.

Funding H.J. is supported by Quantum Science and Technology-National Science and Technology Major Project (grant no. 2024ZD0301000), NSFC (grant no. 12421005) and the Hunan Major Sci-Tech Program (grant no. 2023ZJ1010). Y.-H.M. is supported by NSFC (grant no. 62503497) and the Youth Independent Innovation Fund of AEU (grant no. KYTYJKQTZQ24002). J.-P.X. is supported by NSFC (grant no. 62505360) and Innovation Research Foundation of NUDT (grant no. ZK25-40). R.H. is supported by the RIKEN Special Postdoctoral Researchers (SPDR) program. T.P. is supported by NSFC (grant no. 6207148). Z.-Q.T. is supported by NSFC (grant no. 62375285) and the Science and Technology Innovation Program of Hunan Province (grant no. 2025RC1047).

Competing interests The authors declare no competing interests.

Additional information

Supplementary information The online version contains supplementary material available at https://doi.org/10.1038/s41586-026-10684-4.

Correspondence and requests for materials should be addressed to Yuan-Hao Mao, Ji-Peng Xu, Franco Nori or Hui Jing.

Peer review information *Nature* thanks Mohammad Parvinnezhad Hokmabadi and the other, anonymous, reviewer(s) for their contribution to the peer review of this work. Peer reviewer reports are available.